HHS Public Access

Author manuscript

Sci Transl Med. Author manuscript; available in PMC 2016 June 17.

Published in final edited form as:

Sci Transl Med. 2015 June 17; 7(292): 292ra100. doi:10.1126/scitranslmed.3010611.

Detection of Human Brain Cancer Infiltration *ex vivo* and *in vivo* Using Quantitative Optical Coherence Tomography*

Carmen Kut[1], **Kaisorn L. Chaichana**[2], **Jiefeng Xi**[1], **Shaan M. Raza**[2], **Xiaobu Ye**[2], **Elliot R. McVeigh**[1], **Fausto J. Rodriguez**[3], **Alfredo Quinones-Hinojosa**[#,2], and **Xingde Li**[#,1]

[1]Department of Biomedical Engineering, Johns Hopkins, Baltimore, MD 21205, USA

[2]Department of Neurological Surgery, Johns Hopkins, Baltimore, MD 21287, USA

[3]Division of Neuropathology, Johns Hopkins, Baltimore, MD 21287, USA

Abstract

More complete brain cancer resection can prolong survival and delay recurrence. However, it is challenging to distinguish cancer from non-cancer tissues intraoperatively, especially at the transitional, infiltrative zones. This is especially critical in eloquent regions (e.g. speech and motor areas). This study tested the feasibility of label-free, quantitative optical coherence tomography (OCT) for differentiating cancer from non-cancer in human brain tissues. Fresh *ex vivo* human brain tissues were obtained from 32 patients with grades II-IV brain cancer and 5 patients with non-cancer brain pathologies. Based on volumetric OCT imaging data, pathologically confirmed brain cancer tissues (both high-grade and low-grade) had significantly lower optical attenuation values at both cancer core and infiltrated zones when compared with non-cancer white matter, and OCT achieved high sensitivity and specificity at an attenuation threshold of 5.5 mm^{-1} for brain cancer patients. We also used this attenuation threshold to confirm the intraoperative feasibility of performing *in vivo* OCT-guided surgery using a murine model harboring human brain cancer. Our OCT system was capable of processing and displaying a color-coded optical property map in real time at a rate of 110-215 frames per second, or 1.2-2.4 seconds for an 8-16 mm^3 tissue volume, thus providing direct visual cues for cancer versus non-cancer areas. Our study demonstrates the translational and practical potential of OCT in differentiating cancer from non-cancer tissue. Its

---

*This manuscript has been accepted for publication in Science Translational Medicine. This version has not undergone final editing. Please refer to the complete version of record at www.sciencetranslationalmedicine.org/. The manuscript may not be reproduced or used in any manner that does not fall within the fair use provisions of the Copyright Act without the prior, written permission of AAAS

#To whom correspondence should be addressed: aquinon2@jhmi.edu (A. Q.-H.), xingde@jhu.edu (X.D. L.).

Author contributions: C.K. contributed to the study design, tissue acquisition, execution of experiments, software development, data analysis, and manuscript writing. K.L.C. contributed to the study design, tissue acquisition, and manuscript writing. J.F.X. developed the technology and software for the SS-OCT system. S.M.R. contributed to the study design and tissue acquisition. X.B.Y. contributed to the statistical aspects of the study design. E.R.M. contributed to the study design, data analyses, and manuscript editing and proofreading. F.J.R. performed histology and gold standard determination of all tissue samples. A.Q-H. contributed to the study design, human tissue acquisition, and manuscript editing and proofreading. X.D.L. contributed to the study design, technology development, and manuscript editing and proofreading.

Competing interests: We have filed an international patent application (PCT/US15/22432) entitled “Quantitative tissue property mapping for real-time tumor detection and interventional guidance” (C.K., K.L.C, J.X., E.R.M., A.Q-H., and X.D.L).

Data and materials availability: Raw data not included in this manuscript can be made available upon reasonable request.

intraoperative use may facilitate safe and extensive resection of infiltrative brain cancers and consequently lead to improved outcomes when compared with current clinical standards.

Introduction

Patients with brain cancer have finite survival times with inevitable recurrence and subsequent death, and surgery is the first-line therapy. The median survival time for patients with high-grade brain cancer is approximately 14 months, but individual survival is heterogeneous (1, 2). There is a growing body of evidence showing that the extent of resection is the most important risk factor associated with delayed tumor recurrence and prolonged survival (1-4). However, surgery-inflicted neurological deficits are associated with poorer survival; therefore, it is imperative to achieve extensive resection of cancer tissue without compromising non-cancer tissue (5). In particular, there is great utility in detecting cancer infiltration within white matter, especially because intraoperative deep white matter stimulation can be unreliable and current technologies are sub-optimal in providing a real-time, efficient, and quantitative detection of cancer versus non-cancer white matter.

Various technological advances have made major contributions in surgery, including intraoperative magnetic resonance imaging (MRI) and computed tomography (CT), ultrasound, Raman spectroscopy, and fluorescence-guided resections; but these technologies have pros and cons in providing quantitative, real-time, and three-dimensional continuous guidance in brain cancer detection (6-10). The performances of these different technologies in guiding surgical resection of brain cancer are detailed in table S1.

Optical coherence tomography (OCT) is a non-invasive, label-free, and cost-effective technique capable of imaging tissues in three dimensions in real time (table S1). OCT has been used previously to image various tissue pathologies in human and animal organs, including the retina, gastric tract, coronary artery, breast, and brain (11-13). In recent years, OCT has attracted increasing interest in its application for brain cancer detection and surgical guidance as it can provide high-resolution and continuous, quantitative feedback to the surgeons with imaging depth in millimeters (which is comparable with the resection depth for brain cancers near eloquent areas) (14). For example, OCT has been used *ex vivo* for two-dimensional imaging of human brain cancer tissues (13, 15, 16), as well as *en face* imaging of three-dimensional human brain cancer *ex vivo* (17). Despite these advances, there have been no 3D OCT imaging studies that provide quantitative diagnostic criteria in identifying brain cancer versus non-cancer. Additionally, studies to date have not been able to provide direct visual cues for surgical guidance in real time (14). As a result, the utility of OCT in detecting and facilitating resection of brain cancer in humans remains unclear.

To bridge the gap between research and clinical use, we systematically investigated the potential of OCT for real-time and label-free imaging. After devising optical attenuation parameters and establishing a diagnostic threshold for pathologically confirmed cases, we applied these in a double-blinded study to identify the detection sensitivity and specificity of OCT. We then moved into rodent models of human brain cancer and applied the same optical attenuation diagnostic threshold during *in vivo* brain surgery. Our study provides a

real-time method to construct a color-coded map that offers direct visual cues to distinguish cancer versus non-cancer at high resolution and with a reasonably large field of view, thus demonstrating the translational potential and practicality of OCT during brain cancer surgery.

Results

OCT imaging of human brain cancer versus non-cancer (white matter) *ex vivo*

Fresh human brain tissues surgically removed from 37 patients (table S2) were scanned over a given volume to generate depth-dependent OCT signal profiles and tissue attenuation values using a swept-source OCT system and miniature handheld imaging probe (fig. 1 and fig. S1). For accurate assessment of the attenuation properties, we developed a method to remove the influence of the depth-dependent effects of the beam profiles (18), where the OCT signal from the brain tissue sample is normalized with the OCT signal from a silicon oxide phantom with known attenuation coefficients.

At the high-speed setting [220,000 A-scans/s for 1024–2048 A-scans per 2D frame; or 110-215 2D frames per second (fps)], our OCT system took 1.2-2.4 s to scan, process, and display OCT imaging and tissue attenuation results for an 8-16 mm^3 tissue block (movie S1). Although the default OCT field of view is set to 8-16 mm^3, we can extend the field of view using a robotic positioning device (fig. S2). Based on OCT results and corresponding histology of the imaged tissues, an optimal attenuation threshold was established for the identification of high-grade (grade IV) and low-grade (grade II) human brain cancer with high detection sensitivity and specificity (fig. 1D). Finally, to facilitate the potential intraoperative use of this technology, OCT images were displayed in intuitive 3D and color-coded optical property maps to reflect tissue attenuation properties (fig. 1E; movie S2).

Optical attenuation differences between human brain cancer and non-cancer

Fresh *ex vivo* human brain tissues in the training dataset (9 high-grade, 2 low-grade, 5 non-cancer) were characterized to establish optical attenuation differences between cancer and non-cancer white matter (fig. 2). There was little to moderate overlap in the distribution of optical attenuation values between non-cancer and cancer (9% vs. 33% overlap for high-grade infiltrated zone versus cancer core, and 6% vs. 37% overlap for low-grade infiltrated zone versus cancer core). To ensure the accuracy of the optical attenuation values, the diagnosis of all cancer versus non-cancer tissues were first confirmed with histopathological analysis by a neuro-pathologist (F.J.R.).

Lower attenuation values for cancer tissues were found in both cancer core and the infiltrated zone when compared with surrounding non-cancer white matter (fig. 2A and 2C). For high-grade, the average optical attenuation value of non-cancer (6.2 mm^{-1}) was significantly higher than infiltrated zone (3.5 mm^{-1}) and cancer core (3.9 mm^{-1}); for low-grade, the average optical attenuation value of non-cancer (6.2 mm^{-1}) was significantly higher than infiltrated zone (2.7 mm^{-1}), but not significantly higher than cancer core (4.0 mm^{1}) (table 1). However, there were no statistically significant attenuation differences for

low-grade versus high-grade in both infiltrated zone (2.7 ± 1.0 versus 3.5 ± 0.8; p = 0.45) and cancer core (4.0 ± 1.4 versus 3.9 ± 1.6; p = 0.94) using Welch's t-test.

From the training dataset, the optimal threshold attenuation value—defined as maximum sensitivity with at least 80% specificity—was found to be 5.5 mm^{-1}. Using this specified threshold, we determined the receiver operating characteristics (ROC) in detecting both high-grade and low-grade brain cancer (fig. 3A). As an example, attenuation results of a brain cancer sample were shown with corresponding histology (fig. 3B). Notably, the attenuation map represents optical properties of a 3D tissue block along the entire imaging depth (1.8 mm), while the corresponding histology images represent a 2D section of this tissue block at a specific depth. During histopathological validation, the pathologist (F.J.R.) reviewed multiple sections at different depths and concluded that the sections showed areas with high cancer density (red regions in attenuation map), areas with medium cancer density (yellow regions in attenuation map), and areas with low cancer density, i.e. diffusely infiltrated area with mostly white matter and some neoplastic cell components (green regions in attenuation map).

Evaluation of the optical attenuation threshold in an independent, blinded study of human brain tissue

Brain tissues were collected from 16 additional patients in the validation dataset with cancer (7 high-grade and 9 low-grade) to determine the sensitivity and specificity of the threshold value in an independent blinded study. OCT imaging was performed and attenuation values were obtained by a researcher blinded to tissue type and grade. Histological diagnosis was obtained by a neuropathologist (F.J.R.) blinded to the OCT results. Using a diagnostic optical attenuation threshold of 5.5 mm^{-1}, the specificity was 100% and the sensitivity was 92% for high-grade patients (n = 7). For low-grade patients (n = 9), the specificity was 80% and the sensitivity was 100% (table S3).

OCT versus surgeon in determining cancer from non-cancer

During surgery and prior to OCT imaging of the tissues from the 16 patients in the validation cohort, the surgeon gave an independent evaluation of the tissue based on gross appearance and all intraoperative surgical navigations, including surgical microscopes and intraoperative MRI. The surgeon's impression on the tissue was then compared directly with the blinded histological diagnosis (i.e. gold standard) for 16 patients. Based on these data, the surgeon's detection specificity/sensitivity was 50%/100% for high-grade brain cancer and 40%/100% for low-grade brain cancer. In comparison, the OCT detection specificity/sensitivity was 100%/92% for high-grade brain cancer and 80%/100% for low-grade brain cancer at a threshold of 5.5 mm^{-1}.

Additional optical attenuation analyses and microscopic information offered by OCT

We used a consolidated dataset (training and validation) to evaluate the optical attenuation differences amongst different sub-groups of low-grade and high-grade cancer (table 2). We found that, regardless of treatment, brain cancers have significantly lower attenuations compared with non-cancer white matter, and there are no significant differences between attenuation in newly diagnosed and recurrent brain cancers (table 2). Moreover, the cancer

core has comparable attenuation with infiltrated zone ($p = 0.51$ for high-grade and $p = 0.80$ for low-grade, Welch's t-test). Lastly, we found that non-cancer gray matter has significantly lower attenuation when compared with high-and low-grade cancer cores, but not with high- or low-grade infiltrated zones (table S4).

In addition to optical attenuation analyses, OCT imaging was able to identify microscopic structures which can complement attenuation data in differentiating cancer from non-cancer white matter (fig. 4). OCT was able to identify necrosis and hypercellularity, which appeared as heterogeneous regions of hypo-intense signals (necrosis) surrounded by hyper-intense signals (hypercellularity) in high-grade cancer, as well as hypercellularity and microcysts in low-grade brain cancer (19).

Although our study primarily focused on the attenuation results of high-grade (grade IV) and low-grade (grade II) brain cancer, as the differentiation of grade III is traditionally difficult and often controversial (20), we also studied the attenuation results for three patients with grade III brain cancer (fig. S3). There was moderate to significant overlap in the distribution of optical attenuation values between non-cancer and grade III brain cancer tissues (24 and 77% overlap in cancer core and infiltrated zone, respectively). Histological validation for the infiltrated zone revealed diffuse cancer infiltration, comprising of primarily non-cancer white matter with some neoplastic cell components. Overall, there was a greater overlap between cancer and non-cancer tissues for grade III brain cancer (when compared to grade II), which could be attributed to the limited sample size for grade III (table 1).

In vivo OCT detection of human brain cancer in a murine model

To test the ability of OCT to detect cancer from non-cancer intraoperatively *in vivo*, 5 mice with two different high-grade human brain cancer xenografts were studied. Mice were implanted with U87 cell line or GBM272, a patient-derived cell line (fig. S4). OCT attenuation maps were acquired and displayed over the resection cavity during surgery, which can resolve cancer versus non-cancer on the scale of 0.004 mm^3 (movies S3 and S4). OCT attenuation maps aided the user in identifying regions of cancer versus non-cancer (white matter) before and after surgery, even for mice that displayed more infiltrative brain cancer characteristics with the patient-derived GBM272 cell line (fig. 5). After imaging, mice brains were resected and the corresponding histological slides were reviewed by a neuro-pathologist (F.J.R.) for validation of the OCT results. These histological slides were sectioned in the same orientation as OCT cross-sectional images (i.e. perpendicular to the tissue surface, or perpendicular to the OCT attenuation map and along the dotted lines in fig. 5B-C). In the post-surgery and control images, residual amounts of cancer (approximately 5-10% of the imaged area) were visible in the histological images.

Discussion

The goal of surgery in many cancers and specifically in brain cancer is to achieve maximal resection of cancer while avoiding non-cancer tissues. There is substantial survival benefit and a strong need in achieving a clean cavity margin (3, 4, 21). Patients who undergo gross total resection for high-grade and low-grade brain cancers have a 200% and 160% increase in median survival, respectively, as compared to those who only undergo subtotal resection

(4, 21-23). Patients who incur surgery-related deficits, however, have a 25% decreased median survival than patients without deficits, regardless of extent of resection (5).

This increasing need to identify cancer tissues readily and intraoperatively has led to the development of different surgical adjuncts including surgical navigation, ultrasound, fluorescence imaging, and intraoperative CT and MRI (6-10). These modalities provide substantial contributions to neurosurgery, and their performance has been summarized in table S1 in terms of resolution, FOV, and other parameters. For example, pre-operative CT/MRI provides excellent global surgical guidance with a whole-brain FOV, but is sensitive to brain shifts and position errors (24). Intraoperative CT/MRI, on the other hand, enables surgeons to intraoperatively assess the resection cavity for residual cancer and often reduces the need for a second resection, but it is expensive, time-consuming, and does not provide continuous, real-time intraoperative guidance. Alternatively, intraoperative ultrasound provides real-time imaging with good penetration depth and FOV, and can identify blood flow; however, it has limited spatial resolution and contrast for brain cancer detection (25). Finally, 5-ALA enables intraoperative, fluorescence guided detection of brain cancer at a wide FOV (for fluorescence applications) and good resolution. Clinical studies have shown an increased extent of resection and improved overall survival using this surface imaging technique (22, 23). Nevertheless, 5-ALA has limited sensitivity in delineating all cancer areas, and 5-ALA uptake can vary based on blood-brain barrier permeability, edema, cellular/vascular proliferation and cancer grade; active research is currently underway in further improving its detection sensitivity, especially in infiltrative areas (26, 27). In addition, other emergent technologies, such as stimulated Raman scattering microscopy, provides impressive subcellular resolution and label-free imaging capabilities (7); however, its imaging depth (∼0.1 mm), FOV (∼0.35 × 0.35 mm), and imaging speed (∼1 fps) remain to be further improved for clinical, intraoperative use. Conversely, visible and near-infrared spectroscopy provides very precise estimation of optical parameters such as scattering, absorption coefficient and anisotropy factors (12), but does not provide sufficiently high resolution for brain cancer applications.

OCT is a modality that complements existing tools and the technology we have developed is more effective than other surgical adjuncts for the specific application to reliably, quantitatively and volumetrically distinguish cancer from non-cancer tissues in real time and with continuous, intraoperative image guidance. OCT relies on the reflections of near-infrared and low coherence light, which allows for its deep penetration (compared to visible light), label-free contrast, high-resolution imaging, and the ability to provide real-time quantitative values for optical attenuation (28); additionally, it is easy to use and provides non-contact imaging which will minimize infection risks for intraoperative use. As a recently developed and cost-effective imaging technology, OCT has attracted increasing interest in its application for brain cancer detection and surgical guidance (13, 15-17, 29-31). For example, several groups have made important contributions in the imaging of human brain cancer from *ex vivo* to *in vivo*, and from imaging animal studies to directly imaging in patients (13, 15, 16, 31).

Our study moves OCT a critical step forward toward routine use in patients by systematically and quantitatively analyzing the performance of OCT in a large number of

high-grade and low-grade brain cancers, providing a high-resolution, color-coded attenuation map for real-time and intuitive identification of brain cancer vs. non-cancer in volumetric samples, which is suitable for continuous guidance of tissue resection. To fully understand these reported outcomes, however, it is important to first understand the biological and physical properties which determine the optical attenuation for a tissue specimen. For most systemic organs, cancers are associated with a higher optical attenuation due to its increased cell density and nuclear-to-cytoplasmic (NC) ratio. For brain cancers, the optical attenuation is governed by two key factors: 1) an increased cell density and NC ratio, which will result in an increase in optical attenuation and more importantly, and 2) the degradation of myelin in white matter during brain cancer infiltration, which will result in a decrease in optical attenuation. Thus, as shown in this and other studies, non-cancer white matter has a higher optical attenuation owing to high myelin content, whereas gray matter has a lower attenuation owing to the absence of myelin (16, 19, 32-35). Moreover, when brain cancer infiltrates into white matter, the invading cancer cells are known to break down and decrease the expression of myelin in white matter (32-34); this lowers the attenuation for both cancer core and infiltrated zone when compared with non-cancer white matter. Consequently, our results are consistent with this reported phenomenon in that non-cancer white matter had significantly higher attenuation when compared with brain cancer tissues (regardless of grade). On the other hand, when brain cancer infiltrates into gray matter (which lacks myelin), optical attenuation is mainly determined by increased cell density and NC ratio; thus, as shown in our study, both cancer core and infiltrated zone had high attenuation when compared with non-cancer gray matter. In addition, the attenuation in the cancer core was comparable with that in infiltrated zone, presumably because the cancer core has higher cell density (which increases attenuation) but more complete breakdown of myelin (which decreases attenuation). Finally, all attenuation results (non-cancer versus cancer, low-grade versus high-grade, cancer core versus infiltrated zone) were largely consistent for both newly diagnosed and recurrent patients. As a result, we are able to detect brain cancer from non-cancer tissues based on optical attenuation properties; thus, OCT has translational potential in guiding surgical resections for primary brain cancer patients, especially with the use of complementary techniques, such as cortical stimulation mapping, to identify normal, eloquent cortex.

Importantly, this study established an OCT diagnostic threshold in detecting cancer versus non-cancer with excellent sensitivity (92-100%) and specificity (80-100%). High-grade brain cancer had a higher OCT detection sensitivity but lower specificity when compared with low-grade, although the differences are likely due to the limited number of tissue samples in each subgroup. Moreover, OCT exhibited comparable sensitivity but significantly greater specificity than the standard of care (100% sensitivity and 40-50% specificity), which is interpreted as the surgeon's perception of cancer based on gross appearance and all available intraoperative surgical navigational systems. In comparison, previous studies showed lower sensitivity (26-87%) and specificity (42-100%) for other imaging technologies, as detailed in table S1 (6-10).

In addition to attenuation and diagnoses, OCT was also able to distinguish histologic cancer features (i.e. microcysts, hypercellularity, and necrosis), which could potentially assist the surgeon in detecting cancer grade since microcysts are generally found in lower-grade brain

cancer, while necrosis and hypercellularity are generally found in higher-grade brain cancer and are not characteristics of normal brain. Furthermore, OCT was able to reliably detect cancer from surrounding non-cancer *in vivo* during surgery in a rodent model of human brain cancer by applying the same attenuation threshold obtained from the *ex vivo* human study. Thus, *in vivo* OCT detection of brain cancer is reliable even in the presence of brain motions, uneven tissue surface and other surgical complications (e.g. bleeding).

OCT represents a promising solution in brain cancer localization and mapping. Nevertheless, it does not provide molecular information. The imaging volume is also sub-optimal for imaging the entire resection cavity. For eventual clinical translation, the OCT imaging area (and volume) can be substantially increased by robotic positioning and co-registering with surgical microscopes (29, 30). OCT can also be integrated with wide-field imaging technologies (e.g. MRI and fluorescence) for complementary image guidance, which will further facilitate safe extensive resections. Moreover, additional processing of OCT images can also yield functional information such as Doppler to detect the presence of major embedded blood vessels and therefore prevent bleeding or stroke-related complications during surgery. Intraoperative OCT imaging will benefit from developing more advanced OCT light sources for further improved imaging speeds (> 400 fps) (36) and/or resolution (< 3 μm) (37).

In summary, OCT could have tremendous translational potential in brain cancer resections. Besides brain cancer, this modality may also be useful for distinguishing cancer from non-cancer tissue for other intra-parenchymal brain cancers including metastatic brain cancer. This study sets the stage for future clinical trials and technological refinement that will ultimately lead to an enabling technology for detecting brain cancer rapidly and efficiently, increasing the extent of resection and thus improving patient survival.

Materials and Methods

Study design

This study evaluates the feasibility of OCT in delineating cancer from non-cancer tissue for human patients undergoing brain surgery (fig. 1). Tissues were obtained using intraoperative MRI-guided surgical navigation for patients with low-grade (grade II glioma) and high-grade (grade IV glioma, or glioblastoma, GBM) brain cancers. OCT cross-sectional images were acquired over the tissue *ex vivo* at a uniform spatial interval of 0.5 mm using a swept-source OCT (SS-OCT) system (fig. S1). Each cross-sectional image was then divided into 3 subsections to obtain 3 attenuation data points. After imaging, the tissues underwent histological preparation and processing, and were reviewed for validation of tissue type and cancer grade. More than 1450 data points were collected from the training dataset (9 high-grade, 2 low-grade, and 5 non-cancer) to establish an optimal attenuation threshold to distinguish cancer versus non-cancer (white matter) based on optical attenuation properties. Using these established values, more than 3200 data points were collected from the validation dataset (7 high-grade, 9 low-grade) for a double-blinded study to establish the sensitivity and specificity of our established attenuation threshold. In other words, we collected 4675 data points from a total of 32 patients for a systematic and quantitative analysis of human brain cancer tissues. Finally, we also recruited 3 grade III glioma patients

for attenuation analyses, and 2 additional grade IV glioma patients for OCT-histology correlations, for a total of 5 additional patients. Patients with grade I gliomas were excluded from the study owing to their typically non-infiltrative nature. Patients were assigned to datasets serially based on the date of surgery. In addition to human data, our study also demonstrated the feasibility of OCT in detecting cancer *in vivo* by collecting data during surgical resection of human brain cancer in murine models. Since the brain cancer implantation and resection protocols were well-established in murine models (38-40), only five mice were selected to provide 15 proof-of-concept datasets for OCT detection of brain cancer under an *in vivo* environment and correlation with histology. A total of 3 OCT datasets were collected from each mouse brain over the 8 mm^3 OCT imaging volumes at the following locations: 1) at a selected cancer site before resection; 2) at the same cancer site after surgery; and 3) at a selected non-cancer site (control) in the contralateral hemisphere of the brain. For each imaging dataset, 52 attenuation data points were collected per OCT cross-sectional image, with 256 OCT cross-sectional images per 8 mm^3 imaging volume.

Human brain cancer and non-cancer samples—For all 37 patients, brain tissues were removed using standard neurosurgical techniques (including microsurgical dissection when necessary and the use of intraoperative surgical navigation). Tissues necessary for clinical diagnosis of the patient were obtained before any excess tissues were sent for research purposes. Non-cancer tissue samples were obtained from control, non-cancer patients who required tissue resection as part of a standard surgical approach for seizure (lobectomy). Tissue samples from brain cancer patients were obtained from the cancer core and infiltrated zone, as categorized by the neurosurgeon (A.Q-H.) and later validated by a neuro-pathologist (F.J.R.). In addition, tissues were also obtained from the resection margins of brain cancer patients that showed normal pathology (<5% cancer cells based on visual estimate). These resection margins from brain cancer patients were either obtained as part of the planned trajectory to the cancer core or along the surgically defined margins at the infiltrated-normal brain interface.

Swept-source optical coherence tomography (SS-OCT) system

A home-built SS-OCT system (fig. S1) was used for imaging all samples, as described in Supplementary Methods.

Imaging and histological correlation

Each tissue was cut into flat homogeneous samples at approximately 50 mm^3 per sample. The tissue surfaces were marked with a 3-mm line using a yellow margin marking dye (MasterTech) for histological registration and correlation. A cover glass was placed to prevent dehydration and to flatten the tissue surface. The tissues were then kept on ice until transfer to the imaging stage. For this, the imaging beam was aligned with the 3 mm yellow line on the tissue. This marked our first OCT scan line and the first cross-sectional (B-scan) OCT image was obtained. Afterwards, cross sectional images were acquired at 0.5 mm intervals along the horizontal plane. The image data were stored digitally in a computer for post-processing and attenuation analyses.

After imaging, tissue samples were placed in 10% neutral buffered formalin overnight. Afterwards, tissue samples were transferred to saline and re-sectioned at the first OCT scan line (yellow line) for histological processing and correlation. Based on histology, all tissue samples were divided into 3 categories (cancer core, infiltrated zone, and non-cancer). Each histological slide contained multiple 5-μm thick H&E-stained tissue samples sectioned at an interval of 0.5 mm per slide, with close correspondence to the OCT cross-sectional images' location and orientation (fig. 1).

Optical attenuation

During quantitative analyses of depth-dependent OCT signals, each OCT image was divided into 1 to 3 sections depending on tissue features and characteristics, such that each section roughly delineated a homogeneous tissue region. The optical attenuation value was computed as described previously (18) and in Supplementary Methods. After quantitative analyses, attenuation coefficients for the biological tissues were grouped into several categories for statistical analyses. These included cancer core, infiltrated zone, and resection margin for cancer patient samples, and non-cancer samples as control.

Diagnostic threshold—Data in the training dataset (n = 16) were used to establish an optimal attenuation threshold that distinguishes cancer versus non-cancer white matter. The distribution of attenuation coefficients of non-cancer versus cancer in cancer cores and infiltrated zones were presented in binned histograms at 0.5 mm^{-1}/bin for high-grade and low-grade cancers. To find the attenuation threshold, sensitivity and specificity were estimated and receiver operating characteristics (ROC) for distinguishing cancer vs. non-cancer were calculated. The sensitivity/specificity values obtained at different attenuation values (0-10 mm^{-1} evaluated at intervals of 0.1 mm^{-1}) were estimated for both high-grade and low-grade tissues. Based on the results, the optimal attenuation threshold was determined based on a threshold value that yielded maximum sensitivity with at least 80% specificity.

Calculating sensitivity and specificity for an established attenuation threshold —Data from 16 patients were used to find the sensitivity and specificity associated with the established attenuation threshold in an independent blinded study. For this part of the study, the user was blinded to tissue type and grade when imaging the tissue samples and calculating the attenuation coefficients. A total of 59 tissue samples (19 high-grade and 40 low-grade) were obtained. To determine the test outcome, a tissue sample (about 50 mm^3) was considered cancer if >50% of the OCT attenuation data points were lower than the threshold value, and considered non-cancer if >50% of the OCT attenuation data points were higher than the threshold value. Histological diagnosis was obtained by a neuro-pathologist (F.J.R.) who was blinded to the OCT results. The tissue was then categorized as either true-positive, true-negative, false-positive or false-negative based on the test outcomes (OCT attenuation data) and the histological diagnosis.

OCT versus surgeon in determining cancer from non-cancer tissue—Diagnostic sensitivity and specificity values for OCT were compared with surgeon identification of brain tissues. True-positive, true-negative, false-positive, or false-negative was derived by

comparing surgeon's impression (i.e. test outcome) with the blinded histological evaluation (i.e. true outcome). In this study, the surgeon's perception of cancer was based on all pre-operative and intraoperative imaging information available (e.g. surgical microscope and intraoperative MRI), in addition to the gross appearance of the tissues resected and the clinical history of the patient.

***In vivo* OCT imaging of mice implanted with human glioblastoma cell lines—** To test the ability of OCT to detect cancer from non-cancer *in vivo*, five, 8-week old, NOD/SCID male mice (Charles River Laboratories) were stereotactically inoculated with cancer cells as previously described (38), but with coordinates X: 3.5, Y: 1.4 and Z: 3.5 based on bregma. In three mice, we injected 10^6 glioblastoma cells from a commercial U87 cell line (ATCC®), which produces mostly spherical brain tumors; in two mice, we injected 10^6 glioblastoma cells from a patient-derived primary stem cell line (GBM272) which is slightly more infiltrative and better replicates the migratory and invasive behavior of cancer cells in glioblastoma patients (fig. S4) (39, 40). The mice underwent cancer resection (38) at 4 weeks post implantation, and OCT images were taken as described in Supplementary Methods (fig. S5).

Statistical analysis—To distinguish cancer from non-cancer white matter from the training dataset, we performed two-sample, one-tailed Student's t-test of unequal variance (or Welch's t-test), with the hypotheses that attenuation values for non-cancer white matter is higher than that of cancer core, infiltrated zone, and/or resection margin tissues. For intergroup analyses based on treatment (newly diagnosed versus recurrent), cancer density (cancer core versus infiltrated zone) and grade (high-grade versus low-grade) for the attenuation data from the combined training and validation datasets, we performed two-sample, two-tailed Welch's t-test with the hypothesis that both groups have equal attenuation values. To detect cancer from non-cancer gray matter for the combined training and validation datasets, we performed two-sample, one-tailed Welch's t-test with the hypothesis that gray matter has lower attenuation compared to both cancer and non-cancer white matter tissues. The alpha value was 0.05 and we assumed a normal Gaussian distribution.

Supplementary Material

Refer to Web version on PubMed Central for supplementary material.

Acknowledgments

We thank our collaborators for their generous help and contribution to this project: D. Herzka for data analyses, A. Olivi, W. Anderson and F. Lenz for clinical support and collaboration, J. Mavadia for technological development/assistance with the OCT imaging system, O. Wijesekera and H. Guerrero-Cazares for the rodent models, J. Rincon-Torroella for MRI acquisition and video production/assistance, S. Manrique and I. J. Torres for MRI acquisition, T. Gao for OCT phantom development, and the tissue handling team for tissue transfers from the operating room to the laboratory (L. Chen, A. Abutaleb, J. C. Martinez, S. Dangelmajer, B. Patel, K. Refaey, T. Buitrago).

Funding: Grants R01NS070024 (A.Q-H.), R01CA120480 (X.D.L.), R01EB007636 (X.D.L.), F30CA183430 (C.K.) as well as the Coulter Foundation (X.D.L. and A.Q.-H.).

References and Notes

1. Lacroix M, Abi-Said D, Fourney DR, Gokaslan ZL, Shi W, DeMonte F, Lang FF, McCutcheon IE, Hassenbusch SJ, Holland E, Hess K, Michael C, Miller D, Sawaya R. A multivariate analysis of 416 patients with glioblastoma multiforme: prognosis, extent of resection, and survival. J Neurosurg. 2001; 95:190–198. [PubMed: 11780887]
2. Sanai N, Polley MY, McDermott MW, Parsa AT, Berger MS. An extent of resection threshold for newly diagnosed glioblastomas. J Neurosurg. 2011; 115:3–8. [PubMed: 21417701]
3. Keles GE, Lamborn KR, Berger MS. Low-grade hemispheric gliomas in adults: a critical review of extent of resection as a factor influencing outcome. J Neurosurg. 2001; 95:735–745. [PubMed: 11702861]
4. McGirt MJ, Chaichana KL, Gathinji M, Attenello FJ, Than K, Olivi A, Weingart JD, Brem H, Quinones-Hinojosa AR. Independent association of extent of resection with survival in patients with malignant brain astrocytoma. J Neurosurg. 2009; 110:156–162. [PubMed: 18847342]
5. McGirt MJ, Mukherjee D, Chaichana KL, Than KD, Weingart JD, Quinones-Hinojosa A. Association of surgically acquired motor and language deficits on overall survival after resection of glioblastoma multiforme. Neurosurgery. 2009; 65:463–469. discussion 469-470. [PubMed: 19687690]
6. Rygh OM, Selbekk T, Torp SH, Lydersen S, Hernes TAN, Unsgaard G. Comparison of navigated 3D ultrasound findings with histopathology in subsequent phases of glioblastoma resection. Acta neurochirurgica. 2008; 150:1033–1042. [PubMed: 18773141]
7. Ji M, Orringer DA, Freudiger CW, Ramkissoon S, Liu X, Lau D, Golby AJ, Norton I, Hayashi M, Agar NY. Rapid, Label-Free Detection of Brain Tumors with Stimulated Raman Scattering Microscopy. Science translational medicine. 2013; 5:201ra119–201ra119.
8. Özduman K, Yıldız E, Dinçer A, Sav A, Pamir MN. Using intraoperative dynamic contrast-enhanced T1-weighted MRI to identify residual tumor in glioblastoma surgery: Technical note. J Neurosurg. 2014; 120:60–66. [PubMed: 24138206]
9. Uhl E, Zausinger S, Morhard D, Heigl T, Scheder B, Rachinger W, Schichor C, Tonn JC. Intraoperative computed tomography with integrated navigation system in a multidisciplinary operating suite. Neurosurgery. 2009; 64:ons231–ons240.
10. Stummer W, Tonn JC, Goetz C, Ullrich W, Stepp H, Bink A, Pietsch T, Pichlmeier U. 5-ALA-Derived Tumor Fluorescence: The Diagnostic Accuracy of Visible Fluorescence Qualities as Corroborated by Spectrometry and Histology and Post-Operative Imaging. Neurosurgery. 2013
11. Fujimoto JG. Optical coherence tomography for ultrahigh resolution in vivo imaging. Nat Biotechnol. 2003; 21:1361–1367. [PubMed: 14595364]
12. Zhang Y, Chen Y, Yu Y, Xue X, Tuchin VV, Zhu D. Visible and near-infrared spectroscopy for distinguishing malignant tumor tissue from benign tumor and normal breast tissues in vitro. Journal of biomedical optics. 2013; 18:077003–077003. [PubMed: 23839487]
13. Böhringer H, Boller D, Leppert J, Knopp U, Lankenau E, Reusche E, Hüttmann G, Giese A. Time-domain and spectral-domain optical coherence tomography in the analysis of brain tumor tissue. Lasers in surgery and medicine. 2006; 38:588–597. [PubMed: 16736504]
14. Keles GE, Lundin DA, Lamborn KR, Chang EF, Ojemann G, Berger MS. Intraoperative subcortical stimulation mapping for hemispheric perirolandic gliomas located within or adjacent to the descending motor pathways: evaluation of morbidity and assessment of functional outcome in 294 patients. J Neurosurg. 2004; 100:369–375. [PubMed: 15035270]
15. Bizheva K, Drexler W, Preusser M, Stingl A, Le T, Budka H, Unterhuber A, Hermann B, PovazË B, Sattmann H. Imaging ex vivo healthy and pathological human brain tissue with ultra-high-resolution optical coherence tomography. Journal of biomedical optics. 2005; 10:011006–0110067.
16. Bohringer HJ, Lankenau E, Stellmacher F, Reusche E, Huttmann G, Giese A. Imaging of human brain tumor tissue by near-infrared laser coherence tomography. Acta neurochirurgica. 2009; 151:507–517. discussion 517. [PubMed: 19343270]

17. Assayag O, Grieve K, Devaux B, Harms F, Pallud J, Chretien F, Boccara C, Varlet P. Imaging of non tumorous and tumorous human brain tissue with full-field optical coherence tomography. NeuroImage: Clinical. 2013
18. Xi J, Chen Y, Li XD. Characterizing optical properties of nano contrast agents by using cross-referencing OCT imaging. Biomedical optics express. 2013; 4:842–851. [PubMed: 23761848]
19. van der Meer FJ, Faber DJ, Aalders MC, Poot AA, Vermes I, van Leeuwen TG. Apoptosis- and necrosis-induced changes in light attenuation measured by optical coherence tomography. Lasers Med Sci. 2010; 25:259–267. [PubMed: 19756838]
20. Louis DN, Ohgaki H, Wiestler OD, Cavenee WK, Burger PC, Jouvet A, Scheithauer BW, Kleihues P. The 2007 WHO classification of tumours of the central nervous system. Acta neuropathologica. 2007; 114:97–109. [PubMed: 17618441]
21. Chaichana KL, Jusue-Torres I, Navarro-Ramirez R, Raza SM, Pascual-Gallego M, Ibrahim A, Hernandez-Hermann M, Gomez L, Ye X, Weingart JD, Olivi A, Blakeley J, Gallia GL, Lim M, Brem H, Quinones-Hinojosa A. Establishing percent resection and residual volume thresholds affecting survival and recurrence for patients with newly diagnosed intracranial glioblastoma. Neuro-oncology. 2013
22. Valdes PA, Kim A, Brantsch M, Niu C, Moses ZB, Tosteson TD, Wilson BC, Paulsen KD, Roberts DW, Harris BT. delta-aminolevulinic acid-induced protoporphyrin IX concentration correlates with histopathologic markers of malignancy in human gliomas: the need for quantitative fluorescence-guided resection to identify regions of increasing malignancy. Neuro-oncology. 2011; 13:846–856. [PubMed: 21798847]
23. Roberts DW, Valdes PA, Harris BT, Hartov A, Fan X, Ji S, Pogue BW, Leblond F, Tosteson TD, Wilson BC, Paulsen KD. Adjuncts for maximizing resection: 5-aminolevuinic acid. Clin Neurosurg. 2012; 59:75–78. [PubMed: 22960516]
24. Spivak CJ, Pirouzmand F. Comparison of the reliability of brain lesion localization when using traditional and stereotactic image-guided techniques: a prospective study. J Neurosurg. 2005; 103:424–427. [PubMed: 16235672]
25. Selbekk T, Jakola AS, Solheim O, Johansen TF, Lindseth F, Reinertsen I, Unsgard G. Ultrasound imaging in neurosurgery: approaches to minimize surgically induced image artefacts for improved resection control. Acta neurochirurgica. 2013; 155:973–980. [PubMed: 23459867]
26. Montcel B, Mahieu-Williame L, Armoiry X, Meyronet D, Guyotat J. Biomedical Optics, Miami, FL, 26-30 April 2014. Optical Society of America; 2014. p. BS3A. 2.
27. Stummer W, Novotny A, Stepp H, Goetz C, Bise K, Reulen HJ. Fluorescence-guided resection of glioblastoma multiforme utilizing 5-ALA-induced porphyrins: a prospective study in 52 consecutive patients. J Neurosurg. 2000; 93:1003–1013. [PubMed: 11117842]
28. Cobb MJ, Chen Y, Bailey SL, Kemp CJ, Li XD. Non-invasive imaging of carcinogen-induced early neoplasia using ultrahigh-resolution optical coherence tomography. Cancer Biomark. 2006; 2:163–173. [PubMed: 17192069]
29. Kantelhardt S, Finke M, Schweikard A, Giese A. Evaluation of a Completely Robotized Neurosurgical Operating Microscope. Neurosurgery. 2013; 72:A19–A26.
30. Finke M, Kantelhardt S, Schlaefer A, Bruder R, Lankenau E, Giese A, Schweikard A. Automatic scanning of large tissue areas in neurosurgery using optical coherence tomography. The International Journal of Medical Robotics and Computer Assisted Surgery. 2012; 8:327–336.
31. Levitz D, Thrane L, Frosz M, Andersen P, Andersen C, Andersson-Engels S, Valanciunaite J, Swartling J, Hansen P. Determination of optical scattering properties of highly-scattering media in optical coherence tomography images. Optics express. 2004; 12:249–259. [PubMed: 19471531]
32. Alaminos M, Dávalos V, Ropero S, Setién F, Paz MF, Herranz M, Fraga MF, Mora J, Cheung NKV, Gerald WL. EMP3, a myelin-related gene located in the critical 19q13. 3 region, is epigenetically silenced and exhibits features of a candidate tumor suppressor in glioma and neuroblastoma. Cancer Research. 2005; 65:2565–2571. [PubMed: 15805250]
33. Amberger VR, Hensel T, Ogata N, Schwab ME. Spreading and migration of human glioma and rat C6 cells on central nervous system myelin in vitro is correlated with tumor malignancy and involves a metalloproteolytic activity. Cancer Research. 1998; 58:149–158. [PubMed: 9426071]

34. Binder DK, Berger MS. Proteases and the biology of glioma invasion. Journal of neuro-oncology. 2002; 56:149–158. [PubMed: 11995816]

35. Bevilacqua F, Piguet D, Marquet P, Gross JD, Tromberg BJ, Depeursinge C. In Vivo Local Determination of Tissue Optical Properties: Applications to Human Brain. Applied optics. 1999; 38:4939–4950. [PubMed: 18323984]

36. Reznicek L, Klein T, Wieser W, Kernt M, Wolf A, Haritoglou C, Kampik A, Huber R, Neubauer AS. Megahertz ultra-wide-field swept-source retina optical coherence tomography compared to current existing imaging devices. Graefe's Archive for Clinical and Experimental Ophthalmology. 2014:1–8.

37. Xi J, Zhang A, Liu Z, Liang W, Lin LY, Yu S, Li XD. Diffractive catheter for ultrahigh-resolution spectral-domain volumetric OCT imaging. Optics letters. 2014; 39:2016–2019. [PubMed: 24686663]

38. Kauer TM, Figueiredo JL, Hingtgen S, Shah K. Encapsulated therapeutic stem cells implanted in the tumor resection cavity induce cell death in gliomas. Nature neuroscience. 2011; 15:197–204.

39. Yu, Sc; Ping, Yf; Yi, L.; Zhou, Zh; Chen, Jh; Yao, Xh; Gao, L.; Wang, JM.; Bian, Xw. Isolation and characterization of cancer stem cells from a human glioblastoma cell line U87. Cancer letters. 2008; 265:124–134. [PubMed: 18343028]

40. Chaichana KL, Guerrero-Cazares H, Capilla-Gonzalez V, Zamora-Berridi G, Achanta P, Gonzalez-Perez O, Jallo GI, Garcia-Verdugo JM, Quiñones-Hinojosa A. Intra-operatively obtained human tissue: protocols and techniques for the study of neural stem cells. Journal of neuroscience methods. 2009; 180:116–125. [PubMed: 19427538]

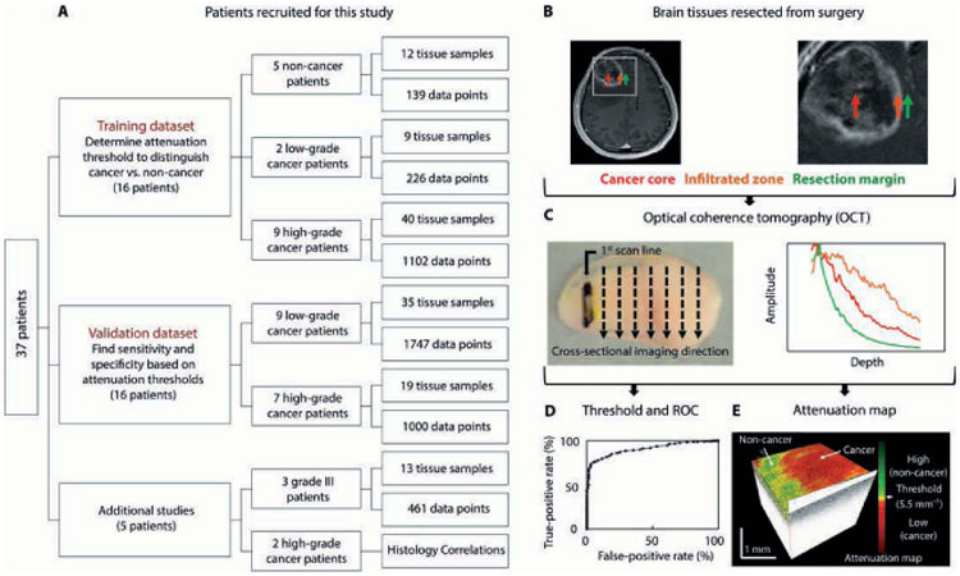

Figure 1. Study design to differentiate cancer versus non-cancer with OCT

We recruited 37 patients for this study, generating over 4670 data points. **(B)** Brain cancer samples were obtained from cancer core (red arrow), infiltrated zone (orange arrow), and resection margin (green arrow) during surgery. **(C)** Tissues were marked with yellow dye (at the 1st scan line) for imaging registration. Cross-sectional OCT imaging of the tissue was then performed along dotted lines. The depth-dependent OCT signal profiles were acquired over different, relatively homogenous regions and analyzed to obtain the optical attenuation values for differentiating cancer versus non-cancer samples. Results showed that OCT signal profiles (curves) and the tissue attenuation values (slope of the curve) differed among cancer core (red), infiltrated zone (orange) and non-cancer resection margin (green). After OCT imaging, tissues were prepared for histology and evaluated by a neuro-pathologist. **(D)** Based on the OCT data, optimal attenuation thresholds and receiver operating characteristics (ROC) curves were determined using brain tissues in the training dataset. Using these parameters, a validation dataset was recruited to establish the OCT sensitivity and specificity in identifying cancer versus non-cancer using a double-blinded procedure. **(E)** To facilitate potential intraoperative use, a 3D volumetric reconstruction of the OCT images was generated with an overlaid color-coded attenuation map of the *ex vivo* human brain tissue.

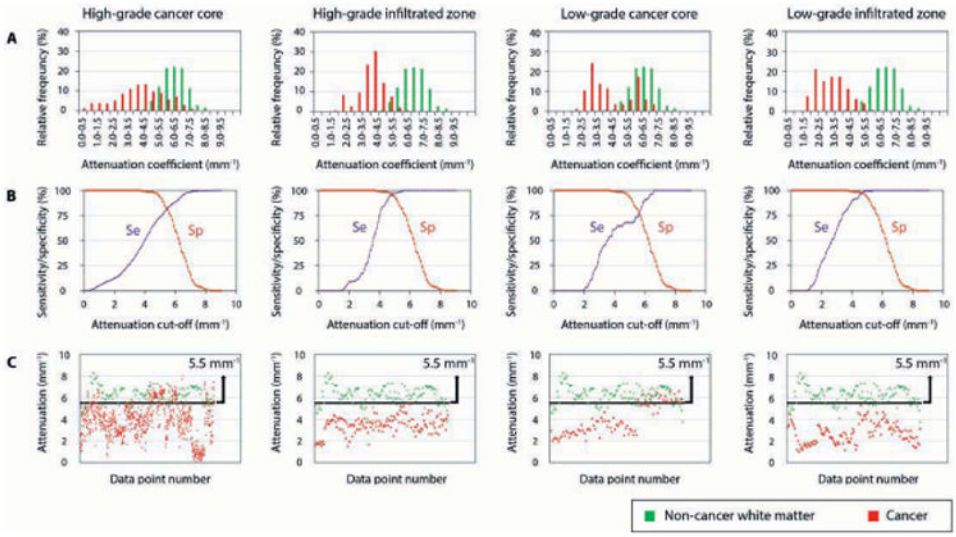

Figure 2. Establishing the optical attenuation threshold for high-grade and low-grade brain cancers in patients

The histogram distribution **(A)**, the diagnostic sensitivity/specificity **(B)**, and the optimal attenuation threshold **(C)** are shown for both cancer core and infiltrated zone in tissue blocks freshly resected from 9 high-grade, 2 low-grade and 5 control patients within the training dataset. At the 5.5 mm^{-1} optical attenuation threshold, maximum sensitivity was achieved while maintaining at least 80% specificity for differentiating cancer versus non-cancer tissues in cancer core and infiltrated zone.

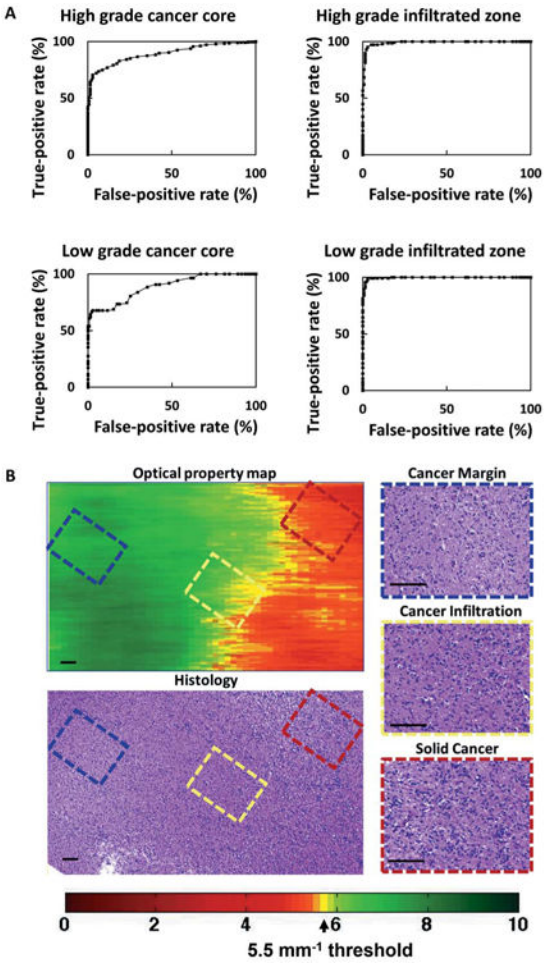

Figure 3. Sensitivity and specificity in cancer core and infiltrated zones and histology correlating with OCT attenuation maps

(A) Receiver operating characteristic (ROC) curves with true-positive (sensitivity) and false-positive (1 - specificity) rates were computed for cancer core and infiltrated zone in tissues obtained from 16 patients within the training dataset. **(B)** *En face* attenuation results of a high-grade brain cancer tissue block (2 mm × 2 mm × 1.8 mm) are shown with corresponding histology. Areas of high cancer density have low optical attenuation (red). Areas of medium cancer density have medium optical attenuation (yellow). Areas with low cancer density (diffusely infiltrated area) have high optical attenuation (green). The corresponding histology, obtained *en face* (same orientation as the attenuation map), was provided for comparison. Scale bars, 100 μm.

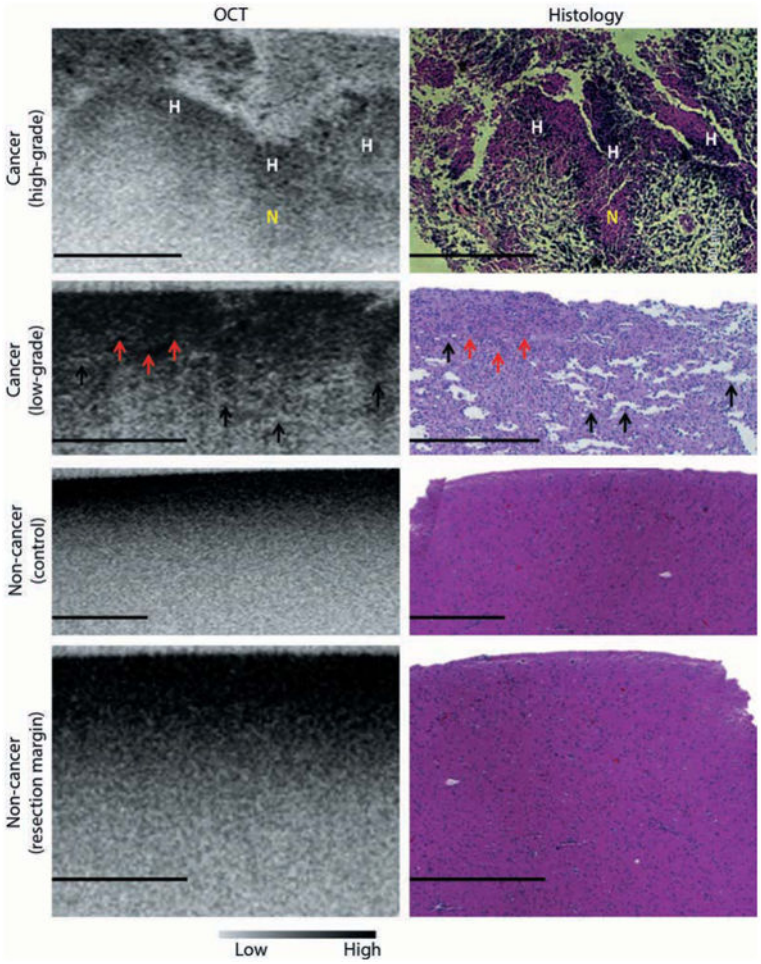

Figure 4. OCT revealed microscopic features that can help distinguish brain cancer versus non-cancer tissue in patients

Cross-sectional OCT images visualized tumor-specific characteristics, such as necrosis (N) and hypercellularity (H), in high-grade brain cancer. Similarly, OCT revealed microcyst formation (black arrows) and hypercellularity (red arrows) in low-grade brain cancer. In contrast, non-cancer white matter tissues—obtained from resected tissues from a seizure patient (control) and from the resection margin of a brain cancer patient—appeared homogeneous with high attenuation on OCT images. Scale bars, 500 μm.

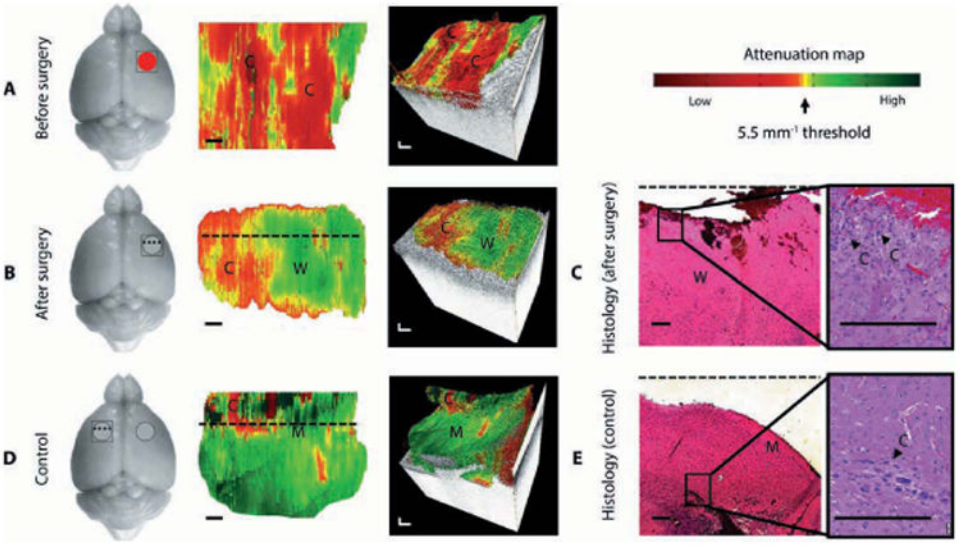

Figure 5. ***In vivoIn vivo*** **brain cancer imaging in a mouse with patient-derived high-grade brain cancer (GBM272)**

(**A** and **B**) Brain tissues were imaged *in vivo* in mice (n = 5) undergoing brain cancer resection. After imaging, the mice were sacrificed and their brains were processed for histology. Here, we show the representative results of a mouse brain at the cancer site before surgery (**A**) and at the resection cavity after surgery (**B**). (**C**) Corresponding histology for the resection cavity after surgery was also shown. (**D** and **E**) With the same mouse, control images were imaged at a seemingly healthy area on the contralateral, left side of the brain (**D**), with its corresponding histology (**E**). The red circle indicates cancer, gray circle indicated resection cavity, and square was the OCT FOV. 2D optical property maps were displayed using an attenuation threshold of 5.5 mm^{-1}. C, cancer; W, noncancer white matter; M, noncancer meninges. Aliasing artifacts at the image boundaries, which were produced when dorsal structures from outside the OCT depth were folded back into the image, were cropped out of image. 3D volumetric reconstructions were overlaid with optical property maps on the top surface. Optical attenuation properties were averaged for each sub volume of 0.326 mm × 0.008 mm × 1.8 mm within the tissue block, with a step size of 0.033 mm in the x direction. Each histological image (**C** and **E**) represented a cross-sectional view of the tissue block: the image corresponds to a single perpendicular slice through the attenuationmap, along the dotted lines in (**B**) and (**D**), respectively. Residual cancer cells were marked with black arrows and correspond to yellow/red regions on the attenuation maps (at the level of the dotted line). Scale bars, 0.2 mm.

Table 1

Attenuation data in the training dataset for patients with high- and low-grade brain cancer

Quantitative attenuation values are provided for 16 patients in the training set (9 high-grade, 2 low-grade, 5 control). *P*-values were calculated using two-sample, one-tailed Welch's t-test based on the hypothesis that non-cancer white matter has higher attenuation.

Tissue	*n*	Attenuation mean ± SD (mm^{-1})	*P*-value (vs. non-cancer tissue)
Control patients (seizure)			
Non-cancer white matter	5	6.2 ± 0.8	N/A
High-grade cancer patients			
Cancer core	9	3.9 ± 1.6	0.002
Infiltrated zone	3	3.5 ± 0.8	0.004
Non-cancer resection margin	4	7.1 ± 1.0	0.902
Low-grade cancer patients			
Cancer core	2	4.0 ± 1.4	0.120
Infiltrated zone	2	2.7 ± 1.0	0.037

Table 2

Optical attenuation differences between treated and untreated brain tissues for patients in the combined training and validation datasets

Data are provided for 32 patients and are reported as averages ± SD. *P*-values were determined using a two-sample, one-tailed Welch's t-test based on the hypothesis that non-cancer white matter (WM) has higher attenuation than cancer and newly diagnosed and recurrent brain tissues have equal attenuation, respectively.

Tissue	*n*	Attenuation (mm^{-1})	*P*-value (vs. non-cancer WM)	*P*-value (new vs. recurrent)
Control patients (seizure)				
Non-cancer white matter	5	6.2 ± 0.8	N/A	N/A
High-grade patients (newly diagnosed)				
Cancer core	9	3.6 ± 1.6	< 0.001	0.225
Infiltrated zone	3	3.7 ± 1.3	0.030	N/A
Non-cancer resection margin	5	6.4 ± 1.0	0.368	0.835
High-grade patients (recurrent)				
Cancer core	6	4.6 ± 1.4	0.022	0.225
Infiltrated zone	1	3.7 ± 0.7	N/A	N/A
Non-cancer resection margin	2	6.2 ± 1.0	0.500	0.835
Low-grade patients (newly diagnosed)				
Cancer core	10	3.8 ± 1.3	<0.001	N/A
Infiltrated zone	4	3.6 ± 1.3	0.005	N/A
Non-cancer resection margin	3	5.9 ± 1.1	0.353	N/A
Low-grade patients (recurrent)				
• Cancer core	1	3.2 ± 0.5	N/A	N/A
• Infiltrated zone	1	3.6 ± 1.6	N/A	N/A